Return of the Big Glitcher: *NICER* timing and glitches of PSR J0537−6910

Wynn C. G. Ho[1,*], **Cristóbal M. Espinoza**[2], **Zaven Arzoumanian**[3], **Teruaki Enoto**[4], **Tsubasa Tamba**[5], **Danai Antonopoulou**[6], **Michał Bejger**[6], **Sebastien Guillot**[7,8], **Brynmor Haskell**[6], **Paul S. Ray**[9]

[1]Department of Physics and Astronomy, Haverford College, 370 Lancaster Avenue, Haverford, PA, 19041, USA [2]Departamento de Física, Universidad de Santiago de Chile, Avenida Ecuador 3493, 9170124 Estación Central, Santiago, Chile [3]X-Ray Astrophysics Laboratory, NASA Goddard Space Flight Center, Greenbelt, MD, 20771, USA [4]Extreme Natural Phenomena RIKEN Hakubi Research Team, RIKEN Cluster for Pioneering Research, 2-1 Hirasawa, Wako, Saitama, 351-0198, [5]Department of Physics, University of Tokyo, 7-3-1 Hongo, Bunkyo-ku, Tokyo, 113-0033, Japan [6]Nicolaus Copernicus Astronomical Center, Polish Academy of Sciences, ul. Bartycka 18, 00-716 Warsaw, Poland [7]IRAP, CNRS, 9 avenue du Colonel Roche, BP 44346, F-31028 Toulouse Cedex 4, France [8]Université de Toulouse, CNES, UPS-OMP, F-31028 Toulouse, France [9]Space Science Division, U.S. Naval Research Laboratory, Washington, DC, 20735, USA

Abstract

PSR J0537−6910, also known as the Big Glitcher, is the most prolific glitching pulsar known, and its spin-induced pulsations are only detectable in X-ray. We present results from analysis of 2.7 years of *NICER* timing observations, from 2017 August to 2020 April. We obtain a rotation phase-connected timing model for the entire timespan, which overlaps with the third observing run of LIGO/Virgo, thus enabling the most sensitive gravitational wave searches of this potentially strong gravitational wave-emitting pulsar. We find that the short-term braking index between glitches decreases towards a value of 7 or lower at longer times since the preceding glitch. By combining *NICER* and *RXTE* data, we measure a long-term braking index $n = -1.25 \pm 0.01$. Our analysis reveals 8 new glitches, the first detected since 2011, near the end of *RXTE*, with a total *NICER* and *RXTE* glitch activity of 8.88×10^{-7} yr^{-1}. The new glitches follow the seemingly unique time-to-next-glitch—glitch-size correlation established previously using *RXTE* data, with a slope of 5 d μHz^{-1}. For one glitch around which *NICER* observes two days on either side, we search for but do not see clear evidence of spectral nor pulse profile changes that may be associated with the glitch.

*wynnho@slac.stanford.edu.

This paper has been typeset from a TEX/LATEX file prepared by the author.

1 INTRODUCTION

With a spin frequency $\nu \approx 62$ Hz (spin period $P \approx 16$ ms), PSR J0537–6910 is the fastest-rotating young pulsar known and is located in the 1–5 kyr old supernova remnant N157B (Wang & Gotthelf 1998; Chen et al. 2006) in the Large Magellanic Cloud at a distance of 49.6 kpc (Pietrzy ski et al. 2019). Its spin rate is only measurable at X-ray and gamma-ray energies up to ~60 keV (Marshall et al. 1998; Kuiper & Hermsen 2015), and the pulsar has the highest spin-down energy loss rate $= 4.9 \times 10^{38}$ erg s^{-1} among more than 2800 known pulsars (Manchester et al. 2005). While the pulsar's spin frequency decreases over the entire 13 years of *RXTE* observation from 1999–2011 at a rate $\dot{\nu} \approx -1.99 \times 10^{-10}$ Hz s^{-1}, PSR J0537–6910 underwent a remarkable 42 or 45 spin-up glitches, yielding an average glitch rate of > 3.2 yr^{-1} (Marshall et al. 2004; Middleditch et al. 2006; Antonopoulou et al. 2018; Ferdman et al. 2018), and its glitch sizes are larger than those seen in most glitching pulsars (Espinoza et al. 2011; Yu et al. 2013; Fuentes et al. 2017; Ho et al. 2020). Because of its high glitch activity, PSR J0537–6910 proves to be extremely useful in theoretical understanding of the mechanism that produces glitches (Link et al. 1999; Melatos et al. 2008; Andersson et al. 2012; Chamel 2013; Ho et al. 2015), which is thought to be due to unpinning of superfluid vortices in the star's crust and possibly its core (Anderson & Itoh 1975; Alpar et al. 1984).

What makes PSR J0537–6910 even more extraordinary is the predictability of when its glitches occur. Middleditch et al. (2006); Antonopoulou et al. (2018); Ferdman et al. (2018) measure a linear correlation between glitch size ν and time to next glitch, with a slope of ~ 0.2 μHz d^{-1} and prediction accuracy of days (see Section 4.2). Such a clear correlation does not seem to hold for any other pulsar and may be unique to PSR J0537–6910 (Melatos et al. 2018). Fuentes et al. (2019) find the large glitches of the Vela pulsar show a weak correlation, Akbal et al. (2017) predict Vela glitch times to an accuracy of about ±0.4 yr, and Melatos & Drummond (2019) predict the next glitch for three other pulsars but with large uncertainties of ±0.7, 4, and 5 yr. Furthermore, statistical analyses give some indication that glitch sizes and times to next glitch each show a bimodal distribution in the case of PSR J0537–6910 (Howitt et al. 2018). Glitch times also appear quasi-periodic (Middleditch et al. 2006; Melatos et al. 2008).

PSR J0537–6910 is of additional interest because of its potential as a source of detectable gravitational waves (GWs). The frequencies at which PSR J0537–6910 might emit GWs are in the most sensitive frequency band of ground-based detectors (around 100 Hz; Abbott et al. 2019c). There is also tantalizing but speculative evidence shown by Andersson et al. (2018) for the generation of GWs in this pulsar by a stellar oscillation, i.e., r-mode oscillation (Andersson 1998; Friedman & Morsink 1998; Andersson & Kokkotas 2001). The most sensitive searches for continuous GW emission from known pulsars use

contemporaneous electromagnetic observations to track a pulsar's spin evolution and thereby reduce the large parameter space of a search (Abbott et al. 2019c). Such a targeted search has not been done in the advanced detector era for PSR J0537–6910 (cf. narrow-band search; Fesik & Papa 2020a,b) because of the lack of a timing model to compare to GW data, and an accurate phase-connected model is not possible over long times without monitoring because of the pulsar's high glitch rate.

With the demise of *RXTE* in 2012, the 42 glitches of PSR J0537–6910 measured by Ferdman et al. (2018) or 45 glitches measured by Antonopoulou et al. (2018) are all the ones obtainable from existing data prior to *NICER*; the difference in glitch numbers is due to small glitches just above or below detection thresholds. *NICER* began observing PSR J0537–6910 soon after launch in 2017 June. As we show here, *NICER* clearly detects the pulsar's spin rate, with typical pulse time-of-arrival (TOA) uncertainties ($< 100 \, \mu s$) generally better than those obtained using *RXTE*. In Section 2, we describe *NICER* observations of PSR J0537–6910 and timing analysis of these observations. In Section 3, we present our timing model and measurements of braking indices of PSR J0537–6910. In Section 4, we discuss measured glitches and their properties. In Section 5, we summarize and discuss some implications of our results.

2   *NICER* DATA

We process and filter *NICER* data on PSR J0537–6910 using HEASoft 6.22–6.26 and NICERDAS 2018-03-01_V003-2020-01-08_V006c. We exclude all events from "hot" detector 34, which gives elevated count rates in some circumstances, and portions of exposure accumulated during passages through the South Atlantic Anomaly. While *NICER* is sensitive to 0.25–12 keV photons, we make an energy cut and extract only events from 1–7 keV, where pulsations are easily detected (see, e.g., Marshall et al. 1998; Kuiper & Hermsen 2015). We ignore time intervals of enhanced background affecting all detectors by constructing a light curve binned at 16 s and removing intervals strongly contaminated by background flaring when the count rate exceeds 10 c s^{-1}. *NICER* experienced a time stamp anomaly which resulted in incorrect time stamps for data taken with MPU1 between 2019 July 8 and 23; we follow the recommended procedure for excluding MPU1 data within this time window1. Using these filtering criteria, we obtain clean data with count rates ~ 3 c s^{-1} for use in pulse timing analysis. We do not conduct spectral analyses using *NICER* data, except for a small subset (see Section 4.3), since the large non-imaging field of view implies an extracted spectrum that will primarily be due to that of the supernova remnant and such spectra from X-ray imaging telescopes are presented in other studies (Chen et al. 2006; Kuiper & Hermsen 2015).

We combine sets of individual ObsIDs into merged observations, with each merged observation yielding a single time-of-arrival (TOA) measurement. ObsIDs are combined such that there is sufficient exposure to confidently detect the spin frequency of PSR J0537–6910, with typical total exposures of 4–9 ks (see below), and merged ObsIDs are those acquired usually within a 3–4 day span and on rare occasions within 6–7 days. We obtain 95

---

[1] https://heasarc.gsfc.nasa.gov/docs/nicer/data_analysis/nicer_analysis_tips.html

merged observations for the data and timespan (2017 August 17 to 2020 April 25) presented here2. Before performing a pulsation search, we use barycorr to transform between Terrestrial Time, used for event time stamps, and Barycentric Dynamical Time (TDB). We adopt the JPL DE421 solar system ephemeris and the *Chandra* sky position of PSR J0537–6910 measured by Townsley et al. (2006), i.e., R.A. = $05^{\mathrm{h}}37^{\mathrm{m}}47^{\mathrm{s}}.416$, decl. $= -69°10'19''.88$ (J2000); note the $0''.4 \pm 0''.2$ (1σ) difference in position from that measured by Chen et al. (2006).

Acceleration searches are conducted using PRESTO (Ransom et al. 2002), with searches using a time bin of 0.5 ms and usually including 8 harmonics given the narrow pulse profile of PSR J0537–6910 (see, e.g., Section 4.3). Pulsations at the spin frequency ($\nu \approx 61.9$ Hz) are almost always the strongest detected. Data are folded at the candidate pulse frequency using prepfold and a refined frequency is determined. On occasion, further iterations are performed to obtain a more robust measurement. Figure 1 shows the difference between the candidate spin frequency measurement from each merged observation and a simple linear model of frequency evolution, $\nu_4 + \dot{\nu}_4(t - t_4)$, arbitrarily set to values obtained from the fourth segment of data. The slope evident in some segments is due to a difference in actual $\dot{\nu}$ for that segment. Each segment is separated by the occurrence of a glitch. Finally, we determine the TOA for each merged observation by cross-correlation with a template pulse profile generated from fitting a Gaussian to a series of *NICER* pulse profiles of PSR J0537–6910. Figure 2 shows the measured uncertainty of each TOA (top panel) and total exposure time of each merged observation that is used for each TOA measurement (bottom panel).

3 SPIN EVOLUTION

3.1 Timing model

We use TEMPO2 (Hobbs et al. 2006) to fit TOAs in each segment between glitches with a timing model that includes a fiducial phase and the pulsar spin frequency ν and its first and second time derivatives, $\dot{\nu}$ and $\ddot{\nu}$, as free parameters. However, for segments 0, 1, and 5, we fix $\ddot{\nu}$ at 10^{-20} Hz s^{-2} [i.e., mean value during segments between glitches in the *RXTE* era (Antonopoulou et al. 2018) and is generally consistent with our *NICER* measurements] because there are insufficient numbers of TOAs to fully constrain the model. Furthermore, for segment 1 when we only have 3 TOAs, ν and $\dot{\nu}$ are determined by searching within a range of values and selecting those that yield the lowest root-mean-square (RMS) residuals. Specifically, the search is performed centred at the first candidate ν measurement in the segment (see Figure 1) and at the $\dot{\nu}$ expected from the general long-term trend (see Figure 4), with search radii of 2 μHz and 1×10^{-13} Hz s^{-1}. Quoted uncertainties correspond to half the range of values covered by all solutions that yield a RMS lower than 75 μs, which is the largest measured TOA uncertainty in segment 1. The results of these timing model fits are given in Table 1, with quoted uncertainties being the formal 1σ errors from the fits. Figures

---

[2]The first NICER observations of PSR J0537–6910 with significant exposure time occur in 2017 July. While we are able to construct 3 TOAs from these observations, we are unable to obtain a sensible phase-connection between these TOAs and others that follow them. This may be due to a small magnitude glitch (with $\nu < 0.06$ μHz) between MJDs 57963 and 57984, but we are unable to determine this conclusively or characterize this possible glitch because of the insufficient number of TOAs provided by the 2017 July data.

3 and 4 show the spin frequency ν and its time derivative $\dot\nu$ for each segment, as well as interglitch values measured using *RXTE*.

The timing solutions determined above provide an initial estimate of glitch sizes. Each glitch is measured more precisely by fitting a timing model (see, e.g., Edwards et al. 2006) that includes glitch parameters ϕ, ν, $\dot\nu$, and $\ddot\nu$ to the set of TOAs that immediately precedes the glitch and the set of TOAs that immediately follows the glitch (e.g., TOAs from segments 0 and 1 are fit to obtain parameters of glitch 1); like glitches detected using *RXTE* (Antonopoulou et al. 2018), an exponential recovery-term is not needed to describe our measured glitches (see also Section 4.1). However, for glitch 1, $\dot\nu$ is not varied during the fitting but is calculated by comparing $\dot\nu$ from segments 0 and 1 at the glitch epoch; its uncertainty is the uncertainty of $\dot\nu$ in segment 1. Because $\dot\nu$ cannot be varied for segment 1, the uncertainty of $\ddot\nu$ for glitch 2 is set to the uncertainty of $\ddot\nu$ for segment 1. For glitches 1 and 5, $\ddot\nu$ is set to zero during the fitting because $\ddot\nu$ is not determined in segments 1 and 5 (see above); for the same reason, $\ddot\nu$ for glitch 2 (and 6) is simply the change from the fixed $\ddot\nu = 10^{-20}$ Hz s^{-2} in segment 1 (and 5) to the measured $\ddot\nu$ in segment 2 (and 6). Glitch epochs are set at the centre of the interval between the last TOA before the glitch and the first TOA after the glitch, and the uncertainty is set at half this interval. The results of these timing model fits are given in Table 2.

The glitch parameters determined above are used together to create a single timing solution for all measured TOAs. The reference time is set at the centre of segment 0, and the reference ν, $\dot\nu$ and $\ddot\nu$ are set at corresponding values for segment 0. The resulting best-fit timing model has a RMS fit residual of 141 μs, i.e., < 0.9 percent of the rotation cycle of PSR J0537–6910. The glitch parameters obtained by this subsequent fit agree within errors to those measured by individual fits above (see Table 2). Figure 5 shows the residual of each TOA after removing the final best-fit timing model.

3.2 Long and short-term braking indices

The spin-down behavior of a pulsar can be described by the braking index, which is defined as $n \equiv \nu\ddot\nu/\dot\nu^2$ and follows from characterizing the spin-down rate as a power law $\dot\nu \propto -\nu^n$. In the case of PSR J0537–6910, its spin-down rate is measured to be increasing ($\dot\nu$ becoming more negative) over time, with Antonopoulou et al. (2018) finding $\ddot\nu = (-7.7 \pm 0.3) \times 10^{-22}$ Hz s^{-2} and $n = -1.22 \pm 0.04$ and Ferdman et al. (2018) finding $\ddot\nu = (-8.2 \pm 0.3) \times 10^{-22}$ Hz s^{-2} and $n = -1.28 \pm 0.04$.

We perform a simple linear fit of $\dot\nu$ over time, which yields $n = -1.32 \pm 0.02$ for only *RXTE* data (taken from Table 1 of Antonopoulou et al. 2018) and $n = -1.4 \pm 0.2$ for only *NICER* data (see Table 1); 1σ errors are obtained by increasing all individual $\dot\nu$ errors by a single factor such that the fit produces a χ^2/dof = 1. A fit of all $\dot\nu$ values gives $\ddot\nu = (-8.00 \pm 0.08) \times 10^{-22}$ Hz s^{-2}, which is shown in Figure 4, and long-term braking index $n = -1.25 \pm 0.01$.

The long-term spin-down behavior of PSR J0537–6910 is in sharp contrast to the behavior over short interglitch intervals. Between individual glitches, the interglitch braking index n_{ig} is generally non-negative and much greater than the canonical value of 3 for spin-down by electromagnetic dipole radiation (see Table 1 and Antonopoulou et al. 2018; see also

Middleditch et al. 2006). Furthermore, Andersson et al. (2018) show that, when measuring braking indices as a function of time since the preceding glitch, n_{ig} tends to decrease toward an asymptotic value. Figure 6 shows *NICER* values alongside *RXTE* values. It is likely that large braking indices determined at short times after a glitch reflect the impact of the glitch on the spin-down behavior of the pulsar. This is borne out in modeling of post-glitch relaxation, with an exponential timescale of 17–34 d and an asymptotic $n_{ig} \approx 7$ (Andersson et al. 2018; Antonopoulou et al. 2018; Ferdman et al. 2018). Observationally, a more reliable measure of spin-down behavior with less glitch contamination can be obtained by determining braking indices at long times after a large glitch. While our current *NICER* dataset contributes only seven new interglitch braking indices, we see that *NICER* values of n_{ig} follow the same trend as those from *RXTE* and are highlighted by interglitch segment 2 which follows 103 ± 11 d after the second largest glitch observed in PSR J0537–6910 (glitch 2; see Table 2). We perform a simple fit with the form $n_{ig} = n_{ig}^{\infty} + n_0 e^{-t/\tau_{ig}}$, where n_0 and τ_{ig} are fit parameters and n_{ig}^{∞} is the asymptotic value of the braking index which we take to be either 3, 5, or 7; fits yield decay timescales of 19–44 d, with a longer timescale for a lower braking index (see Figure 6). While assuming an asymptotic $n_{ig}^{\infty} = 7$ leads to a better fit than assuming $n_{ig}^{\infty} = 3 \text{ or } 5$, the frequent occurrence of glitches may be preventing measurements of $n_{ig} < 7$. We discuss implications of braking indices of 5 and 7 in Section 5.2.

4 GLITCHES

4.1 Glitch properties

The detection of these 8 glitches, with parameters given in Table 2, in 2.7 yr of observation yields a glitch rate of 3.0 yr^{-1}. Thus PSR J0537–6910 continues to glitch at the same rate as during the *RXTE* era, when either 42 glitches (Ferdman et al. 2018) or 45 glitches (Antonopoulou et al. 2018) are found in 12.95 yr of *RXTE* data at a rate of either 3.24 yr^{-1} or 3.47 yr^{-1}, respectively.

Glitching activity of a pulsar can also be characterized by the parameter $A_g \equiv \sum_i (\Delta v / v)_i / t_{obs}$, where the summation is over each glitch i and t_{obs} is time over which the pulsar is monitored (McKenna & Lyne 1990). For glitches detected using *RXTE* and $t_{obs} = 12.95$ yr, the results of Antonopoulou et al. (2018) yield $\sum_i \Delta v_i = (709.5 \pm 0.8)$ μHz and $A_g = (8.84 \pm 0.01) \times 10^{-7}$ yr^{-1}, while the results of Ferdman et al. (2018) yield $\sum_i \Delta v_i = (707.4 \pm 0.8)$ μHz and $A_g = (8.81 \pm 0.01) \times 10^{-7}$ yr^{-1}. For glitches detected using *NICER* and $t_{obs} = 2.7$ yr, values from Table 2 give $\sum_i \Delta v_i = (153.1 \pm 0.3)$ μHz and $A_g = (9.22 \pm 0.02) \times 10^{-7}$ yr^{-1}. Figure 7 plots the cumulative fractional glitch magnitude $\Delta v / v$ over the *RXTE* and *NICER* eras. Combining *RXTE* and *NICER* glitches produces an activity parameter $A_g = (8.88 \pm 0.01) \times 10^{-7}$ yr^{-1}. We note that Ferdman et al. (2018) find an indication that A_g decreases during the time *RXTE* is monitoring PSR J0537–6910. However, we find that A_g during the *NICER* era is similar to or even greater than A_g measured during the *RXTE* era.

Figure 8 shows measured Δv and $|\dot{v}|$. Middleditch et al. (2006) argue that there exists a hard upper limit of $|\dot{v}| = 1.5 \times 10^{-13}$ Hz s^{-1} based on the first 23 glitches detected using *RXTE*. However, analysis of the next 22 glitches reveal several exceeding this limit, with three even

having $|\dot{\nu}| > 2 \times 10^{-13}$ Hz s^{-1} (Antonopoulou et al. 2018); analysis by Ferdman et al. (2018) find somewhat lower $|\dot{\nu}|$ but still several exceeding the proposed limit. While Antonopoulou et al. (2018) indicate such large $|\dot{\nu}|$ should be rare (based on 3 out of 45), *NICER* data reveals 4 out of 8 glitches with $|\dot{\nu}| > 2 \times 10^{-13}$ Hz s^{-1}, although their uncertainties are large enough to reach below this limit.

The 8 glitches detected using *NICER* show potentially correlated properties, in addition to the same glitch size-time to next glitch correlation observed in *RXTE* glitches (see Section 4.2). *NICER* glitches appear in pairs, with each pair consisting first of a smaller glitch ($\nu \approx 8 - 16 \, \mu$Hz) and then a larger glitch ($\nu \approx 24 - 36 \, \mu$Hz) but each glitch in a pair having similar $\dot{\nu}$ and $|\ddot{\nu}|$ (and $\ddot{\nu} > 0$ for the first glitch in the pair, then $\ddot{\nu} < 0$ for the second glitch in the pair), albeit with large uncertainties (see Table 2 and Figure 8). Each pair occurs quasi-periodically (as is evident from, e.g., Figure 1), with a period of $\sim 210 - 270$ d (in ν) that simply reflects the glitch size-time to next glitch correlation and $\sim 440 - 480$ d (in $\dot{\nu}$). These behaviors do not seem to occur in the *RXTE* era, and it will be interesting to see whether this continues with future monitoring and detection of glitches using *NICER*.

For the three largest glitches (glitches 2, 4, and 6), we add an exponential term in the timing model to look for a potential exponential recovery associated with each glitch. No evidence of exponential recovery for glitch 6 is found, but there is marginal evidence for glitches 2 and 4 (with χ^2/dof decreasing from 4.1 to 2.6 and from 12 to 6.9, respectively), each with a timescale of ~5 d. This is in contrast to the 20 d timescale of the largest *RXTE* glitch (Antonopoulou et al. 2018).

4.2 Glitch predictability

PSR J0537–6910 is unique in how well its glitch sizes ν correlate with time to the next glitch (Middleditch et al. 2006; Antonopoulou et al. 2018; Ferdman et al. 2018). Figure 9 shows this correlation, with *NICER* glitches from Table 2 and *RXTE* glitches from Antonopoulou et al. (2018). We perform two fits to model the correlation: one linear model is constrained such that the time to next glitch is zero when $\nu = 0$ and a second linear model that allows for non-zero time to next glitch when $\nu = 0$. One might argue that the former is more physically-motivated. However, Figure 9 clearly shows that there is a delay even for small glitches, which could suggest that there is a minimum time to next glitch or that the correlation has a different slope or becomes non-linear at small glitch sizes. Results of the fits to all *NICER* and *RXTE* glitches are time to next glitch = 6.4 d (ν/μHz) and time to next glitch = (23 ± 1) d + (5.08 ± 0.07) d (ν/μHz), and both fit results are plotted in Figure 9. Fits to only *NICER* or only *RXTE* glitches yield very similar results, and the above results also closely match those obtained by Antonopoulou et al. (2018); Ferdman et al. (2018) using only *RXTE* glitches.

While these best-fit results indicate a formal uncertainty in time to next glitch of only a few days, comparison of the two fit correlations can produce a difference of ~ 10 d in predicted time, and observed values show significant scatter around the best-fit correlations. To obtain a more reliable estimate of the uncertainty in predicted time to next glitch, we expand the parameter space covered by the best-fit correlation until 68 percent of measured glitches (with a follow-up glitch) fall within the expanded region. In particular, for the fit that is

constrained at $v = 0$, we increment symmetrically the slope around the best fit value until 35 of 51 glitches lie within the two lines defined, i.e., time to next glitch = (6.4 ± 1.5) d $(v/\mu\text{Hz})$. For the fit that is unconstrained at $v = 0$, we increment the normalization rather than the slope and find the two lines defined by time to next glitch = (23 ± 18) d + 5.08 d $(v/\mu\text{Hz})$ encompass 68 percent of glitches. Each of these are illustrated in Figure 9. From these results, the actual uncertainty in time to next glitch is $\sim \pm 20$ d.

4.3 Glitch-induced emission variability

We present a limited search for potential spectral and pulse profile changes associated with a glitch because the large non-imaging field-of-view of *NICER* is not ideal for studying emission from a weak point source embedded within bright diffuse emission, such as the case of PSR J0537–6910. Note that Ferdman et al. (2018) look for but do not find glitch-associated flux and pulse profile changes using the *RXTE* dataset (see also, e.g., Palfreyman et al. 2018 for a radio search during a Vela pulsar glitch, Ray et al. 2019 for a X-ray search during three spin-down glitches of NGC 300 ULX-1, and Feng et al. 2020 for a X-ray polarization search during a Crab pulsar glitch). Here, we identify *NICER* observations that are nearest in time before and after glitch 4 (see Table 2) on MJD 58424 (2018 November 2) and compare spectra and pulse profiles to see if there are any clear signs of variability that could be associated with the glitch. Note that glitch 7 has the next nearest in time observations, about three days on either side of the glitch.

For spectral analysis, ObsID 1020100312 (MJD 58421; October 30) and 1020100313 (MJD 58422; October 31) are taken about two to three days before the glitch and ObsID 1020100314 (MJD 58425; November 3) and 1020100315 (MJD 58426; November 4) are taken about one to two days after the glitch. Data are processed using nicerl2 in NICERDAS with standard filtering options. We apply a barycentric correction, extract spectra from clean event data, subtract a background generated using the niback-gen3C50 tool, and add and bin spectra using mathpha and grppha, respectively. We obtain net exposures of 6.8 ks and 5.3 ks from the above specified pre and post-glitch observations, respectively. A comparison of the spectra results in $\chi^2/\text{dof} = 552/314$ and no distinctive features or clearly visible differences. We also fit each spectrum at 1–5 keV with an absorbed power law model and obtain model parameters before and after the glitch that are consistent within uncertainties, i.e., absorption $N_\text{H} = (2.7 \pm 0.6) \times 10^{21}$ cm^{-2} versus $(2.2 \pm 0.6) \times 10^{21}$ cm^{-2}, power law index $\Gamma = 2.7 \pm 0.1$ versus 2.5 ± 0.1, and unabsorbed flux = $(6.0 \pm 0.2) \times 10^{-12}$ erg s^{-1} cm^{-2} versus $(6.1 \pm 0.2) \times 10^{-12}$ erg s^{-1} cm^{-2}; errors are at 90 percent confidence. Imaging spectra of the supernova remnant using *Chandra* and *XMM-Newton* (Chen et al. 2006; Kuiper & Hermsen 2015) indicate higher N_H (= 6×10^{21} cm^{-2}) but comparable power law index ($\Gamma \sim$ 2.4) and flux ($\approx 1 \times 10^{-11}$ erg s^{-1} cm^{-2}) to our spectral results. Therefore we conclude that our spectra are dominated by remnant emission, and pulsed emission from PSR J0537–6910 would be difficult to extract, which limits our ability to measure glitch-induced spectral variability.

For pulse profile analysis, our data reduction procedure is as described in Section 2 and yields exposures of 7.2 ks and 4.7 ks for the pre and post-glitch observations described above, respectively. We also consider observations from a somewhat larger range of dates

around the glitch epoch. In particular, ObsID 1020100309–1020100311 (MJD 58416–58419; October 25–28) are from before the glitch and ObsID 1020100317–1020100321 (MJD 58431–58436; November 9–14) are from after the glitch, and merged observations from these ObsIDs have exposures of 7.5 ks and 8.4 ks, respectively. Figure 10 shows a comparison of the pulse profiles from before and after the glitch. Like the spectra, there are no clear significant differences. Subtracting from each pulse profile an average pulse profile, constructed from the above observations, we find residuals that are constant within uncertainties and a shift of one phase bin.

5 DISCUSSIONS

In this work, we present results of our ongoing campaign of monitoring and timing the pulsar PSR J0537–6910 using *NICER*. We are able to obtain a rotation phase-connected timing model for the evolution of the pulsar spin frequency v during the first 2.7 yr of *NICER* observations. In agreement with timing results using *RXTE* from 1999–2011, we measure a long-term braking index $n = -1.25 \pm 0.01$ and a short-term braking index between glitches that seems to relax over time towards a value of $n_{ig} = 7$ or possibly lower. We measure 8 glitches, with similar properties as *RXTE* glitches, and the rate is in line with the 42 or 45 glitches measured in 13 years of *RXTE* data. The 8 glitches also show a pairing/periodicity whose significance will be tested by future observations. We obtain a more reliable estimate of the uncertainty in the observed correlation between glitch size and time to next glitch. Finally, for the glitch that was most closely observed in time, i.e., within ± 2 d, we search for but do not see clear evidence of spectral or pulse profile changes that could be associated with the glitch.

We provide here limited discussions of implications of our monitoring results and newly detected glitch activity. This is because much of the timing and glitch behaviors seen using the current *NICER* dataset is in good agreement with the behaviors seen using the *RXTE* dataset, and implications of the latter dataset are described extensively in many previous works (see below).

5.1 Superfluid and crust moment of inertia and pulsar mass

The mechanism that produces large spin-up glitches like those seen in the Vela pulsar (Dodson et al. 2007; Palfreyman et al. 2018) and PSR J0537–6910 is thought to be a sudden transfer of angular momentum from a rapidly rotating superfluid that permeates the neutron star inner crust to the rest of the star, which is slowing down from electromagnetic radiation braking (Anderson & Itoh 1975; Haskell & Melatos 2015; Graber et al. 2017). Link et al. (1999) provide strong support for this theory by first showing that the fractional moment of inertia (I_{sf}/I) of the superfluid angular momentum reservoir is related to a pulsar's glitch activity via $I_{sf}/I \gtrsim 2\tau_c A_g$, where I is total moment of inertia and $\tau_c = -v/2\dot{v}$ is pulsar characteristic age. They then show that the glitch activity of pulsars like Vela gives $I_{sf}/I \gtrsim 0.01$, and this approximately matches the theoretical fractional moment of inertia of a neutron star's crust I_{crust}/I. For PSR J0537–6910, we find $2\tau_c A_g = 0.00874$, which agrees with that found in previous works (Middleditch et al. 2006; Antonopoulou et al. 2018; Ferdman et al. 2018). More recently, calculations by Andersson et al. (2012); Chamel (2013)

indicate that the above relation is underestimated after accounting for superfluid entrainment and should instead be $I_{sf}/I \geq 2\tau_c A_g \langle m_n^* \rangle/m_n$, where $\langle m_n^* \rangle$ and m_n are averaged effective neutron mass and neutron mass, respectively (and $\langle m_n^* \rangle/m_n \approx 4.2$; Chamel 2012), and as a result, the angular momentum required by a glitch is more than the crust can provide. One solution proposed by Andersson et al. (2012) is that the superfluid component in the crust extends into the core. Subsequently, Ho et al. (2015, 2017) show that, by combining a pulsar's glitch activity with a measurement of true age or surface temperature, one can obtain valuable constraints on properties of the superfluid and even measure the mass of the pulsar; for the A_g and estimated age of PSR J0537–6910, the pulsar's mass turns out to be much higher than the canonical $1.4 M_\odot$. Very recently, Sauls et al. (2020) suggest superfluid entrainment may not be as strong as found by Chamel (2012, 2017). More work is needed to resolve the issue.

5.2 Braking index and GW implications

As described in Section 3.2, we determine a long-term spin-rate change $\ddot{\nu} = (-8.00 \pm 0.08) \times 10^{-22}$ Hz s^{-2} from spin-rate $\dot{\nu}$ measurements of PSR J0537–6910 over the past 21 years (Figure 4), which indicates an increasing $|\dot{\nu}|$ over time, unlike for most pulsars. The corresponding braking index $n \equiv \nu\ddot{\nu}/\dot{\nu}^2 = -1.25 \pm 0.01$ is significantly lower than the canonical value of 3, which is implied for a pulsar whose rotational energy loss rate is purely due to electromagnetic dipole radiation (Shapiro & Teukolsky 1983). The braking index of PSR J0537–6910 is the lowest precisely measured value (cf. J1738–2955 has $n = -70 \pm 40$ and J1833ed value ($n = -15 \pm 2$; Parthasarathy et al. 2020). Glitches could contribute to lowering the braking index, as possibly indicated by the prevalence of low n for glitching pulsars (Espinoza et al. 2017; see also Ho 2015). Various other ideas and models that can produce a braking index below 3 have been proposed, e.g., a changing moment of inertia due to superfluidity (Ho & Andersson 2012), evolution of magnetic field orientation (Middleditch et al. 2006; Lyne et al. 2015; Johnston & Karastergiou 2017) or magnetic field strength (Romani 1990), as demonstrated for the case of PSR J0537–6910 (Gourgouliatos & Cumming 2015; Ho 2015), and particle winds (Michel 1969; Michel & Tucker 1969; Tong et al. 2013).

Meanwhile, measurements of the braking index of PSR J0537–6910 over shorter timescales of tens of days between glitches yields much larger values (Table 1). While the long-term spin evolution is clearly affected by glitches, the strength of the effect is unclear. Regardless, one can see that the post-glitch spin behavior appears to relax at long times after a glitch to a braking index value near 7 or even lower (Figure 6; see also Andersson et al. 2018), which is supported by a fit of post-glitch spin-rate with a model that assumes changes on an exponential timescale (see Section 3.2).

In addition to mechanisms that can lead to a braking index less than 3, such as those described above, it is well-known that neutron stars emitting GWs can have a braking index greater than 3. For example, a neutron star with a quadrupolar mass deformation, characterized by an ellipticity $\varepsilon \equiv |I_{xx} - I_{yy}|/I_{zz}$, where I_{xx}, I_{yy}, and I_{zz} are triaxial components of the stellar moment of inertia, can emit GWs at a frequency ν_{gw} ($= 2\nu$) with a strain amplitude

$$h_0 = \frac{16\pi^2 G}{c^4} \frac{\varepsilon I_{zz}}{d} v^2$$
$$= 4.23 \times 10^{-26} \left(\frac{\varepsilon}{10^{-5}}\right)\left(\frac{10\,\mathrm{kpc}}{d}\right)\left(\frac{v}{100\,\mathrm{Hz}}\right)^2 \tag{1}$$

(see, e.g., Abbott et al. 2019c). The GW strain amplitude h_0, which is either measured or has an upper bound in the case of non-detection, can be compared to the "spin-down limit" strain amplitude h_{sd}, such that a constraint on a pulsar's ellipticity is obtained when $h_0/h_{\mathrm{sd}} < 1$. The spin-down limit

$$h_{\mathrm{sd}} = \left(-\frac{5G}{2c^3}\frac{I_{zz}}{d^2}\frac{\dot{v}}{v}\right)^{1/2}$$
$$= 8.06 \times 10^{-26}\left(\frac{10\,\mathrm{kpc}}{d}\right)\left(\frac{100\,\mathrm{Hz}}{v}\right)^{1/2}\left(\frac{-\dot{v}}{10^{-10}\,\mathrm{Hz\,s^{-1}}}\right)^{1/2} \tag{2}$$

is determined by assuming that a neutron star's rotational energy loss is due entirely to GW quadrupolar emission and implies a braking index $n = 5$. As GW searches become more sensitive, such that the measured h_0 decreases, an improving constraint on ellipticity is

$$\varepsilon = 1.91 \times 10^{-5}\left(\frac{100\,\mathrm{Hz}}{v}\right)^{5/2}\left(\frac{-\dot{v}}{10^{-10}\,\mathrm{Hz\,s^{-1}}}\right)^{1/2}\left(\frac{h_0}{h_{\mathrm{sd}}}\right). \tag{3}$$

The latest LIGO/Virgo searches of PSR J0537–6910 find an upper limit of $h_0/h_{\mathrm{sd}} = 1.92$ using GW data from the second observing run (O2), which collected data from 2016 November 30 to 2017 August 25 (Abbott et al. 2019a). Because the only timing model of PSR J0537–6910 available at the time of the GW search is that derived from *RXTE* observations from 1999–2011, the search by Abbott et al. (2019a) could only be conducted in a frequency band around the frequency expected for PSR J0537–6910 and could not account for glitches (Ashton et al. 2017; Keitel et al. 2019). A contemporaneous timing model, such as that determined here using *NICER*, enables the most sensitive targeted searches. Estimating the h_0 sensitivity upper limit of O2 data at $v_{\mathrm{gw}} = 124$ Hz from Figure 2 of Abbott et al. (2019c), such a targeted search could yield $h_0/h_{\mathrm{sd}} < 0.4$, which would set the limit $\varepsilon < 4 \times 10^{-5}$ and limit the percentage of rotational energy loss that is due to GW emission to < 20 percent. We also note that, while PSR J0537–6910 is much more distant than pulsars in the Milky Way, the decrease in signal strength [e.g., equation (1)] is partly compensated by its higher GW frequency, which is in the most sensitive range of ground-based GW detectors.

An alternative GW emission mechanism is that due to fluid motions in a neutron star. For example, an active r-mode oscillation can produce GWs (Andersson 1998; Friedman & Morsink 1998; Andersson & Kokkotas 2001), and GW searches for r-modes in pulsars are ongoing (see, e.g., Abbott et al. 2019b). The GW frequency in the case of r-modes is $v_{\mathrm{gw}} \sim (4/3)v$ [or $v_{\mathrm{gw}} \sim (1.4 - 1.6)v$ after accounting for relativistic corrections; Andersson et al. 2014; Idrisy et al. 2015; Jasiulek & Chirenti 2017; Caride et al. 2019], and the theoretical strain amplitude equivalent to equation (1) is

$$h_0 = 5.36 \times 10^{-26} \left(\frac{\alpha}{10^{-2}}\right)\left(\frac{10\,\text{kpc}}{d}\right)\left(\frac{v}{100\,\text{Hz}}\right)^3, \qquad (4)$$

while the spin-down limit h_{sd} is 3/2 that given by equation (2) (Owen 2010) and leads to a limit on the r-mode amplitude

$$\alpha = 0.02 \left(\frac{100\,\text{Hz}}{v}\right)^{7/2}\left(\frac{-\dot{v}}{10^{-10}\,\text{Hz}\,\text{s}^{-1}}\right)^{1/2}\left(\frac{h_0}{h_{\text{sd}}}\right). \qquad (5)$$

What makes r-modes of special relevance to PSR J0537–6910 is that, if the spin evolution of a neutron star is dominated by GW emission from an active r-mode, then the resulting braking index is 7 (Owen et al. 1998), although it can also be less than 7 (Alford & Schwenzer 2014). As we show in Section 3.2 (see also Andersson et al. 2018; Ferdman et al. 2018), the braking index between glitches of PSR J0537–6910 seems to relax over time towards a value of 7, as effects of the glitch on long-term spin evolution decrease. If correct, this suggests an active r-mode and the spin evolution of PSR J0537–6910 is determined by GW emission. Such a situation is examined in Andersson et al. (2018), who conclude that an active r-mode is marginally possible, especially with uncertainties and discrepancies in our understanding of r-modes and their impact on observations (see, e.g., Ho et al. 2019, and references therein).

Narrow-band searches for GWs generated by r-modes in PSR J0537–6910 have been conducted using O1 and O2 data (Fesik & Papa 2020a,b; see also Caride et al. 2019). We estimate, using the GW h_0 sensitivity upper limit of O2 data at $v_{\text{gw}} \approx 90$ Hz from Abbott et al. (2019c), that an improved targeted search of r-modes in PSR J0537–6910 using a contemporaneous timing model and accounting for glitches would yield $h_0/h_{\text{sd}} < 0.3$, which would set the limit $\alpha < 0.06$ and limit the percentage of rotational energy loss that is due to GW emission to < 10 percent. Efforts are underway to search the latest, most sensitive GW data from the third observing run (O3), which collected data from 2019 April 1 to 2020 March 27. The timing model provided here using *NICER* data, with 3 glitches occurring during O3 (see Figure 8), will produce the best limits on ellipticity and r-mode amplitude of PSR J0537–6910.

ACKNOWLEDGEMENTS

REFERENCES

Abbott et al. 2019a, Phys. Rev. D, 99, 122002

Abbott et al. 2019b, ApJ, 875, 122

Abbott et al. 2019c, ApJ, 879, 10

Akbal O, Alpar MA, Buchner S, Pines D, 2017, MNRAS, 469, 4183

Alford MG, Schwenzer K, 2014, ApJ, 781, 26

Alpar MA, Pines D, Anderson PW, Shaham J, 1984, ApJ, 276, 325

Anderson PW, Itoh N, 1975, Nature, 256, 25

Andersson N, 1998, ApJ, 502, 708

Andersson N, Kokkotas KD, 2001, International Journal of Modern Physics D, 10, 381

Andersson N, Glampedakis K, Ho WCG, Espinoza CM, 2012, Phys. Rev. Lett, 109, 241103 [PubMed: 23368300]

Andersson N, Jones DI, Ho WCG, 2014, MNRAS, 442, 1786

Andersson N, Antonopoulou D, Espinoza CM, Haskell B, Ho WCG, 2018, ApJ, 864, 137

Antonopoulou D, Espinoza CM, Kuiper L, Andersson N, 2018, MNRAS, 473, 1644

Ashton G, Prix R, Jones DI, 2017, Phys. Rev. D, 96, 063004

Caride S, Inta R, Owen BJ, Rajbhandari B, 2019, Phys. Rev. D, 100, 064013

Chamel N, 2012, Phys. Rev. C, 85, 035801

Chamel N, 2013, Phys. Rev. Lett, 110, 011101 [PubMed: 23383772]

Chamel N, 2017, Journal of Low Temperature Physics, 189, 328

Chen Y, Wang QD, Gotthelf EV, Jiang B, Chu Y-H, Gruendl R, 2006, ApJ, 651, 237

Dodson R, Lewis D, McCulloch P, 2007, Ap&SS, 308, 585

Edwards RT, Hobbs GB, Manchester RN, 2006, MNRAS, 372, 1549

Espinoza CM, Lyne AG, Stappers BW, Kramer M, 2011, MNRAS, 414, 1679

Espinoza CM, Lyne AG, Stappers BW, 2017, MNRAS, 466, 147

Feng H, et al., 2020, Nature Astronomy, 4, 511

Ferdman RD, Archibald RF, Gourgouliatos KN, Kaspi VM, 2018, ApJ, 852, 123

Fesik L, Papa MA, 2020a, ApJ, 895, 11

Fesik L, Papa MA, 2020b, ApJ, 897, 185

Friedman JL, Morsink SM, 1998, ApJ, 502, 714

Fuentes JR, Espinoza CM, Reisenegger A, Shaw B, Stappers BW, Lyne AG, 2017, A&A, 608, A131

Fuentes JR, Espinoza CM, Reisenegger A, 2019, A&A, 630, A115

Gourgouliatos KN, Cumming A, 2015, MNRAS, 446, 1121

Graber V, Andersson N, Hogg M, 2017, International Journal of Modern Physics D, 26, 1730015

Haskell B, Melatos A, 2015, International Journal of Modern Physics D, 24, 1530008

Ho WCG, 2015, MNRAS, 452, 845

Ho WCG, Andersson N, 2012, Nature Physics, 8, 787

Ho WCG, Espinoza CM, Antonopoulou D, Andersson N, 2015, Science Advances, 1, e1500578 [PubMed: 26601293]

Ho WCG, Espinoza CM, Antonopoulou D, Andersson N, 2017, in Kubono S, Kajino T, Nishimura S, Isobe T, Nagataki S, Shima T, Takeda Y, eds, 14th International Symposium on Nuclei in the Cosmos (NIC2016). p. 010805 (arXiv:1703.00932), doi:10.7566/JPSCP.14.010805

Ho WCG, Heinke CO, Chugunov AI, 2019, ApJ, 882, 128

Ho WCG, Jones DI, Andersson N, Espinoza CM, 2020, Phys. Rev. D, 101, 103009

Hobbs GB, Edwards RT, Manchester RN, 2006, MNRAS, 369, 655

Howitt G, Melatos A, Delaigle A, 2018, ApJ, 867, 60

Idrisy A, Owen BJ, Jones DI, 2015, Phys. Rev. D, 91, 024001

Jasiulek M, Chirenti C, 2017, Phys. Rev. D, 95, 064060

Johnston S, Karastergiou A, 2017, MNRAS, 467, 3493

Keitel D, et al., 2019, Phys. Rev. D, 100, 064058

Kuiper L, Hermsen W, 2015, MNRAS, 449, 3827

Link B, Epstein RI, Lattimer JM, 1999, Phys. Rev. Lett, 83, 3362

Lyne AG, Jordan CA, Graham-Smith F, Espinoza CM, Stappers BW, Weltevrede P, 2015, MNRAS, 446, 857

Manchester RN, Hobbs GB, Teoh A, Hobbs M, 2005, AJ, 129, 1993

Marshall FE, Gotthelf EV, Zhang W, Middleditch J, Wang QD, 1998, ApJ, 499, L179

Marshall FE, Gotthelf EV, Middleditch J, Wang QD, Zhang W, 2004, ApJ, 603, 682

McKenna J, Lyne AG, 1990, Nature, 343, 349

Melatos A, Drummond LV, 2019, ApJ, 885, 37

Melatos A, Peralta C, Wyithe JSB, 2008, ApJ, 672, 1103

Melatos A, Howitt G, Fulgenzi W, 2018, ApJ, 863, 196

Michel FC, 1969, ApJ, 158, 727

Michel FC, Tucker WH, 1969, Nature, 223, 277

Middleditch J, Marshall FE, Wang QD, Gotthelf EV, Zhang W, 2006, ApJ, 652, 1531

Owen BJ, 2010, Phys. Rev. D, 82, 104002

Owen BJ, Lindblom L, Cutler C, Schutz BF, Vecchio A, Andersson N, 1998, Phys. Rev. D, 58, 084020

Palfreyman J, Dickey JM, Hotan A, Ellingsen S, van Straten W, 2018, Nature, 556, 219 [PubMed: 29643483]

Parthasarathy A, et al., 2020, MNRAS, 494, 2012

Pietrzy ski G, et al., 2019, Nature, 567, 200 [PubMed: 30867610]

Ransom SM, Eikenberry SS, Middleditch J, 2002, AJ, 124, 1788

Ray PS, et al., 2019, ApJ, 879, 130

Romani RW, 1990, Nature, 347, 741

Sauls JA, Chamel N, Alpar MA, 2020, arXiv e-prints, p. arXiv:2001.09959

Shapiro SL, Teukolsky SA, 1983, Black holes, white dwarfs, and neutron stars : the physics of compact objects. Wiley

Tong H, Xu RX, Song LM, Qiao GJ, 2013, ApJ, 768, 144

Townsley LK, Broos PS, Feigelson ED, Garmire GP, Getman KV, 2006, AJ, 131, 2164

Wang QD, Gotthelf EV, 1998, ApJ, 494, 623

Yu M, et al., 2013, MNRAS, 429, 688
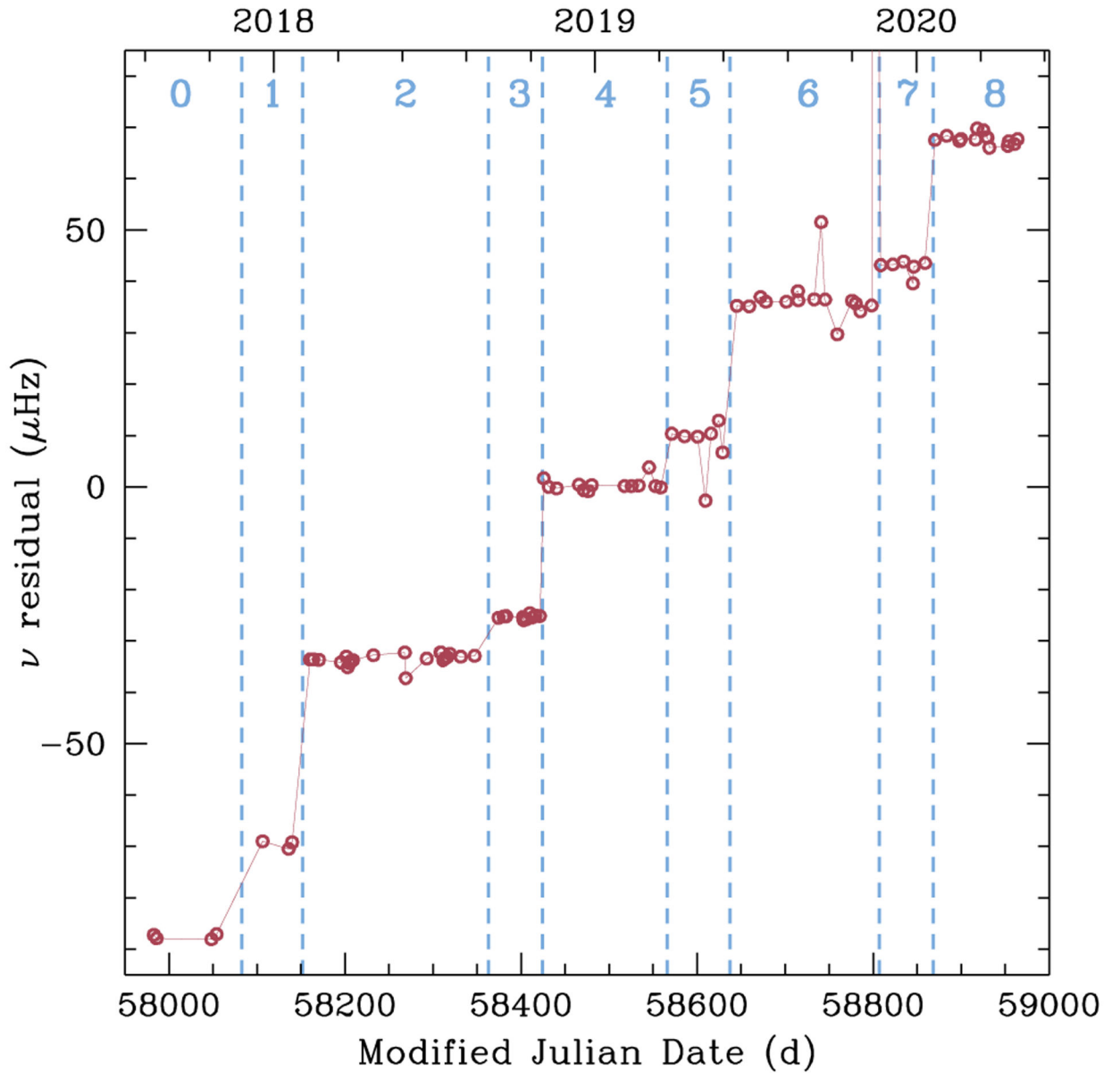
Figure 1.
Difference between the measured candidate spin frequency of PSR J0537–6910 and linear model for frequency evolution, $\nu_4 + \dot{\nu}_4(t - t_4)$, where ν_4 and $\dot{\nu}_4$ are values from segment 4 at t_4 = MJD 58493 (see Table 1). Segments are labeled by numbers and separated by the occurrence of a glitch, each of which is denoted by a vertical dashed line.
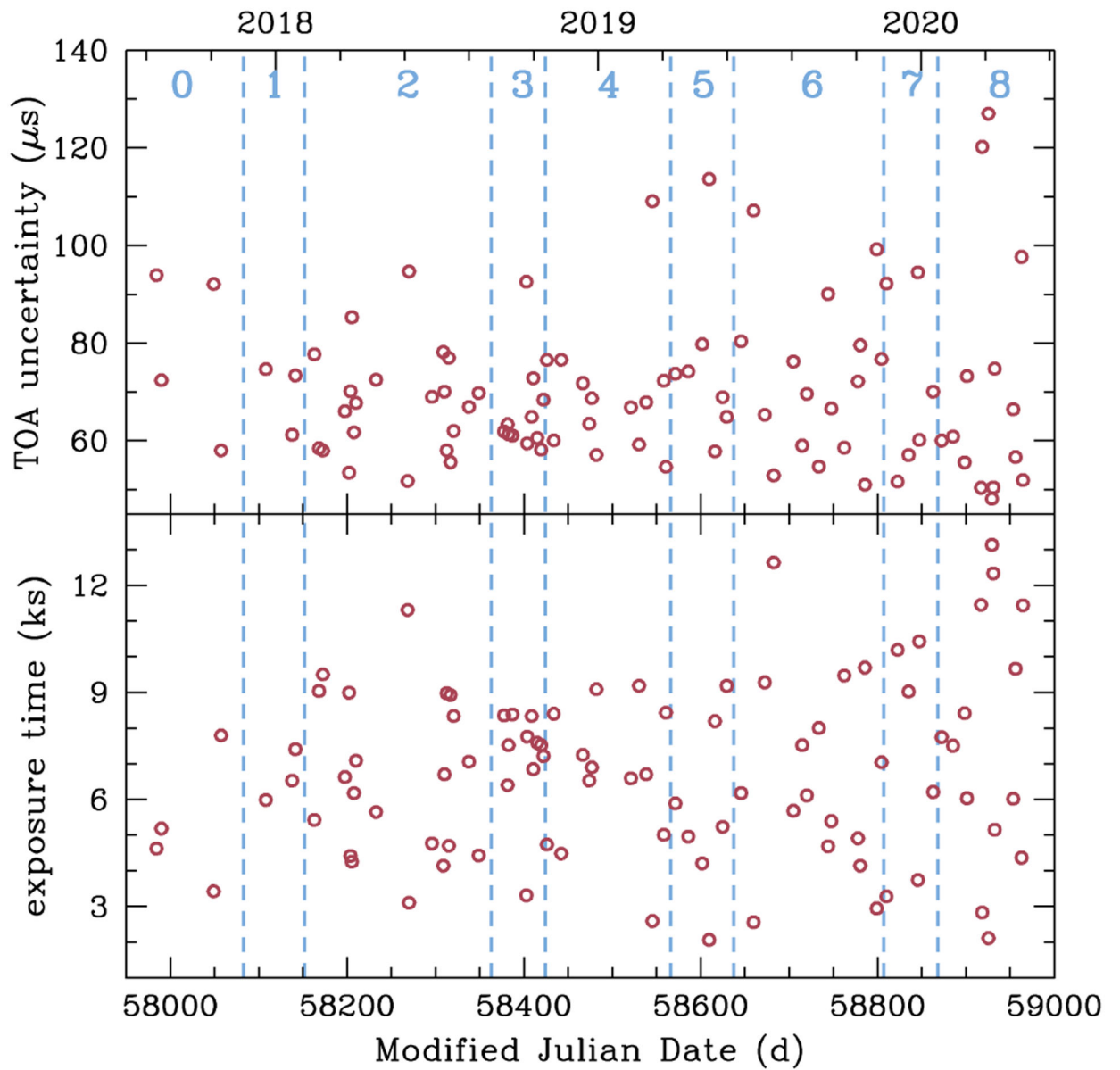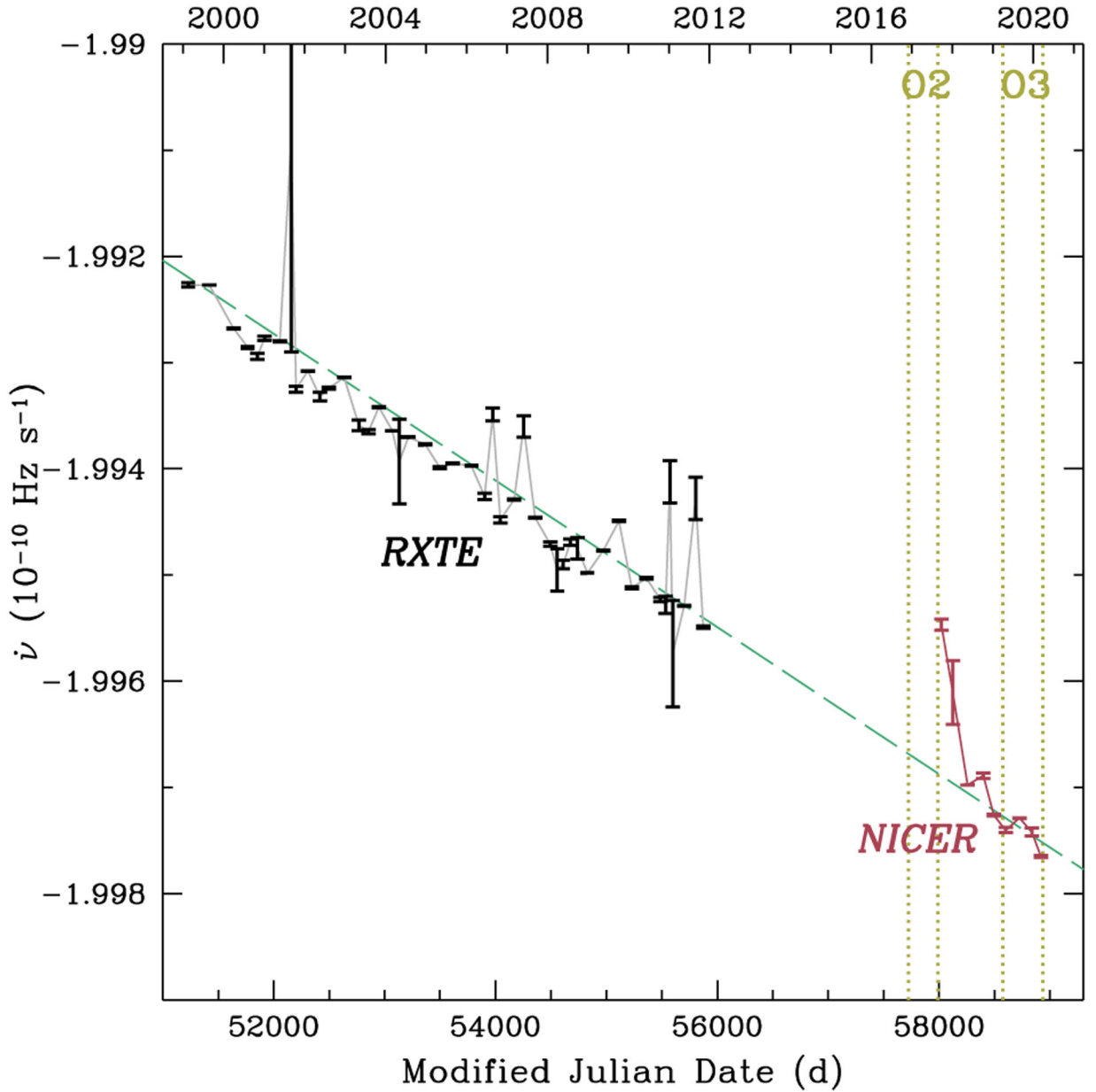
Figure 2.
Uncertainty in measured time-of-arrival (top) and total exposure time (bottom) for each merged observation. Segments are labeled by numbers and separated by the occurrence of a glitch, each of which is denoted by a vertical dashed line.
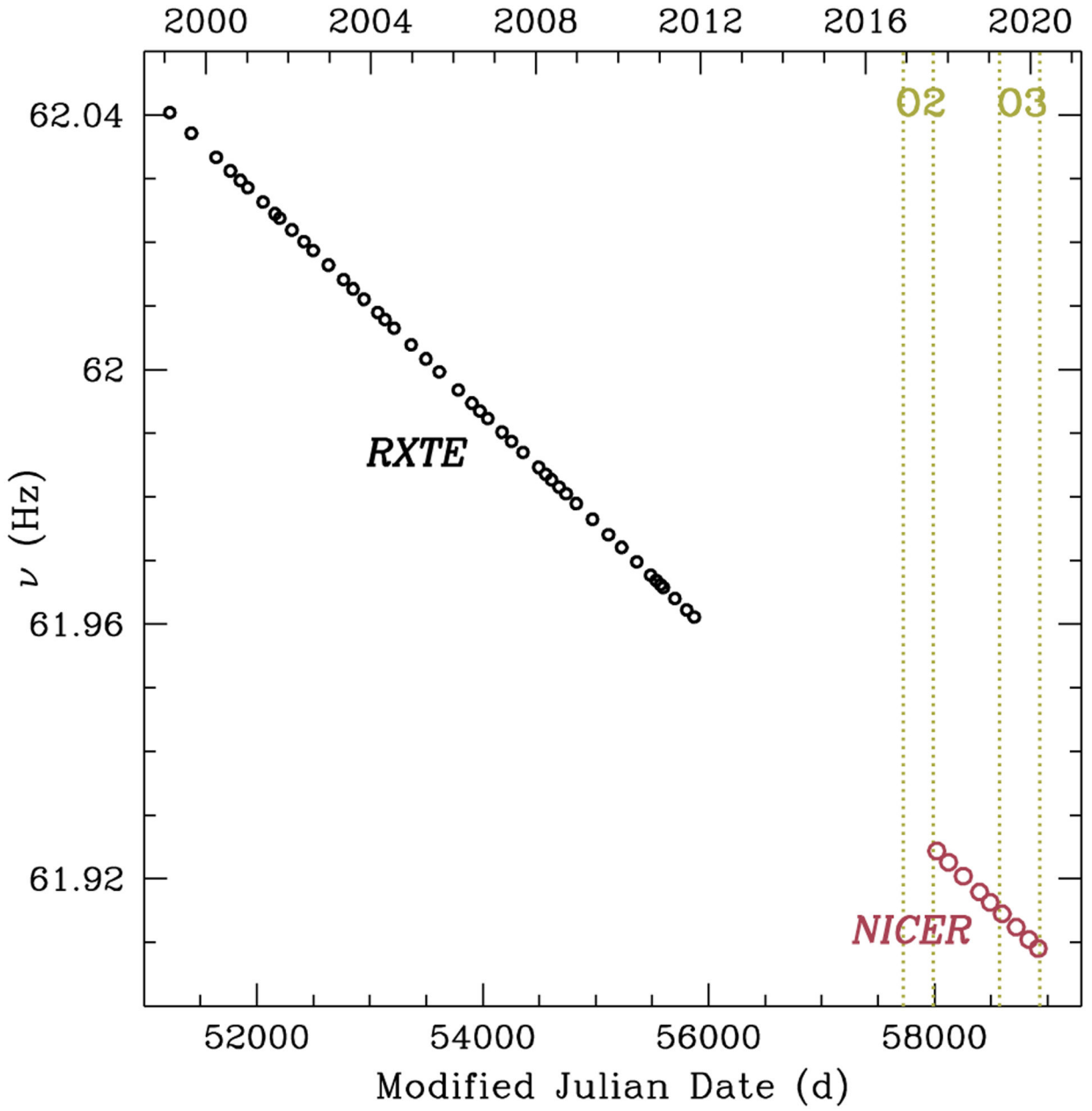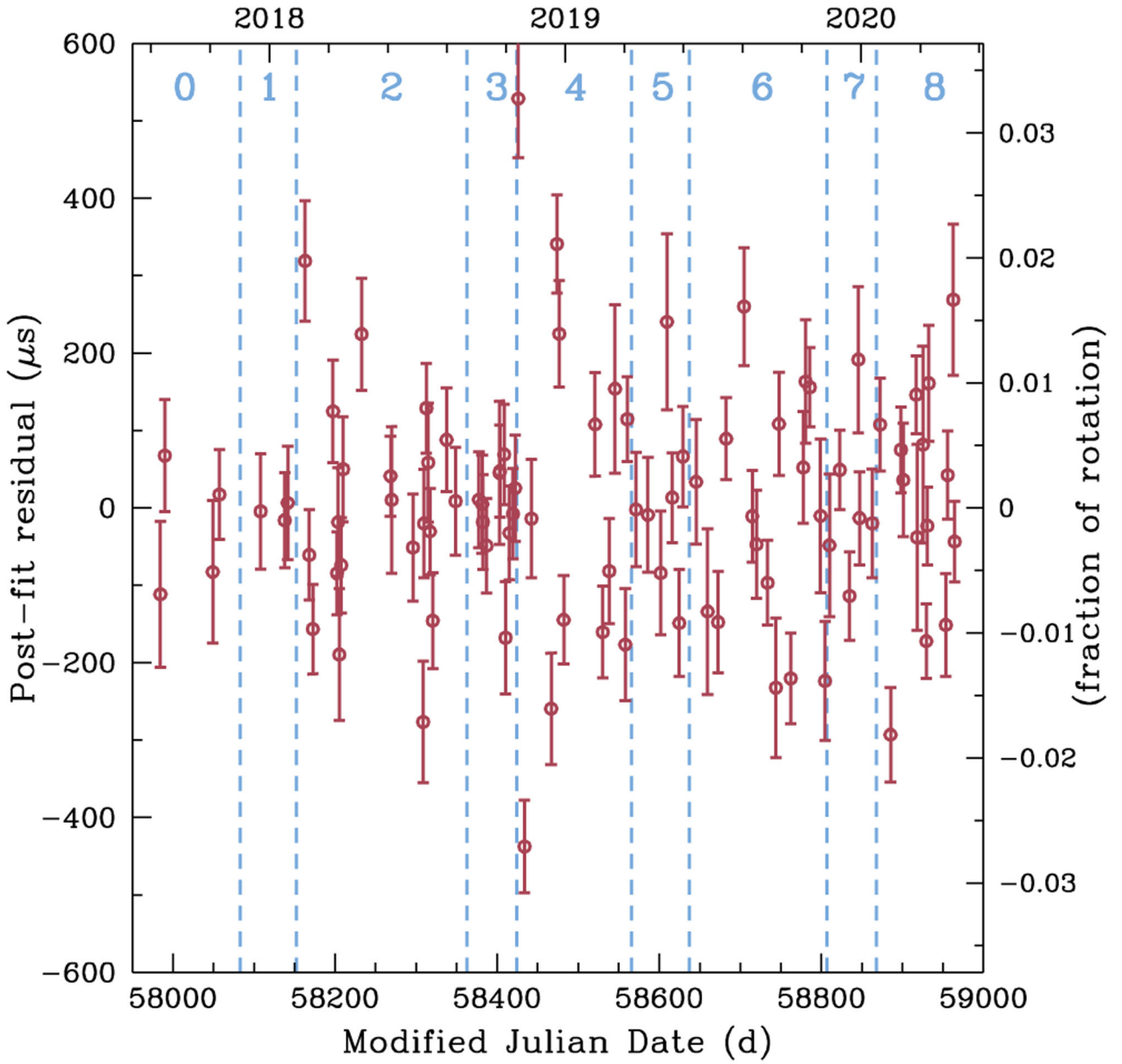
Figure 3.
Evolution of the spin frequency ν of PSR J0537–6910. Large circles are NICER values measured by fitting a timing model to TOAs in each segment (see Table 1). Small circles denote RXTE values from Table 1 of Antonopoulou et al. (2018). Vertical dotted lines denote the start (MJD 57722, 2016 November 30) and end (MJD 57990, 2017 August 25) of the second observing run (O2) and start (MJD 58574, 2019 April 1) and end (MJD 58935, 2020 March 27) of the third observing run (O3) of LIGO/Virgo.

Figure 4.
Evolution of the spin frequency time derivative $\dot{\nu}$ of PSR J0537–6910. NICER values are measured by fitting a timing model to TOAs in each segment (see Table 1). RXTE values are from Table 1 of Antonopoulou et al. (2018). Errors are 1σ uncertainty. Dashed line shows a linear fit of NICER and RXTE data with best-fit $\ddot{\nu} = -8.00 \times 10^{-22}$ Hz s^{-2}. Vertical dotted lines denote the start (MJD 57722, 2016 November 30) and end (MJD 57990, 2017 August 25) of the second observing run (O2) and start (MJD 58574, 2019 April 1) and end (MJD 58935, 2020 March 27) of the third observing run (O3) of LIGO/Virgo.
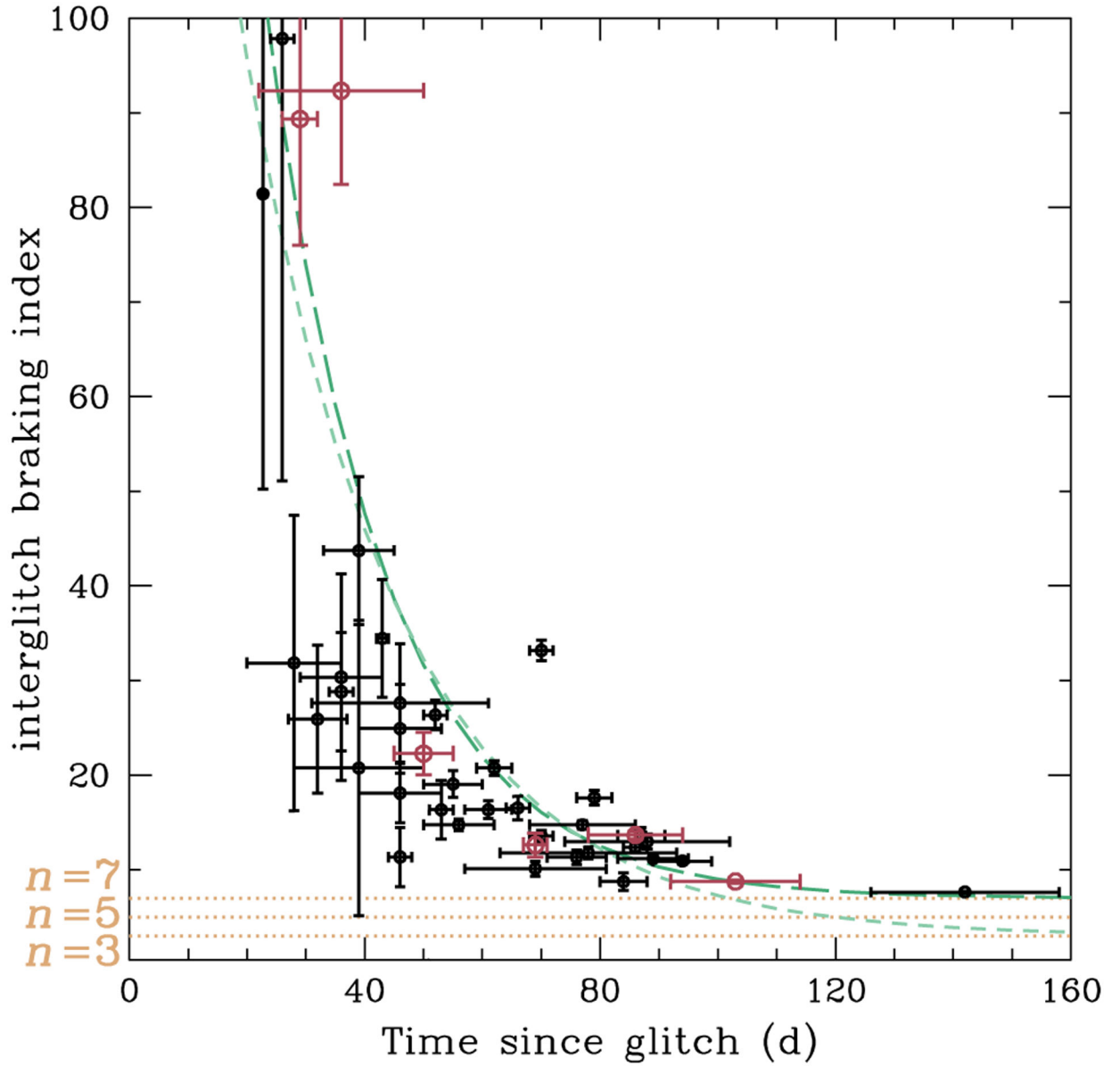
Figure 5.
Timing residual for each merged observation after accounting for the best-fit timing model, with left axis in μs and right axis in fraction of rotation cycle. Errors are 1σ uncertainty. Segments are labeled by numbers and separated by the occurrence of a glitch, each of which is denoted by a vertical dashed line.
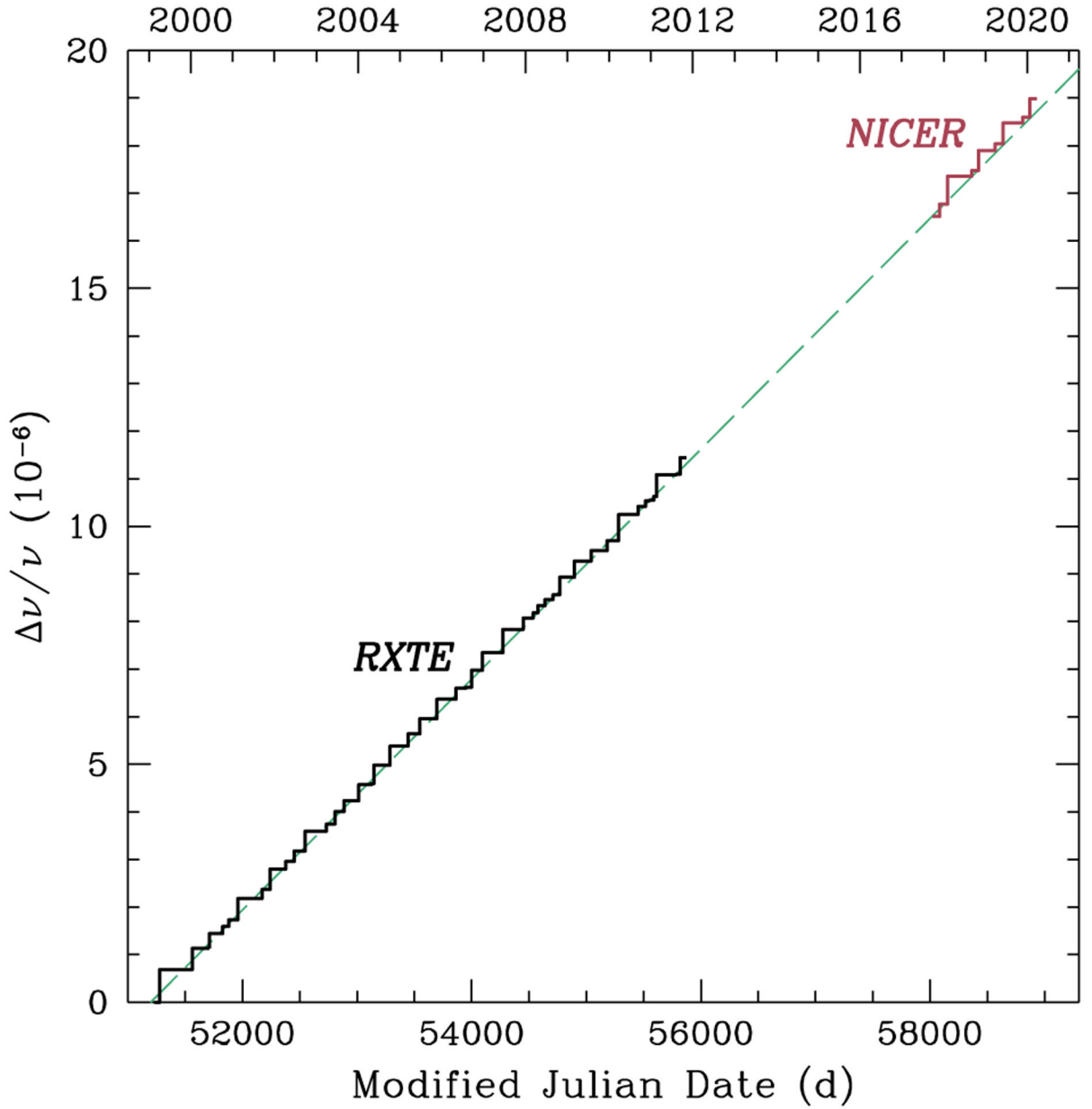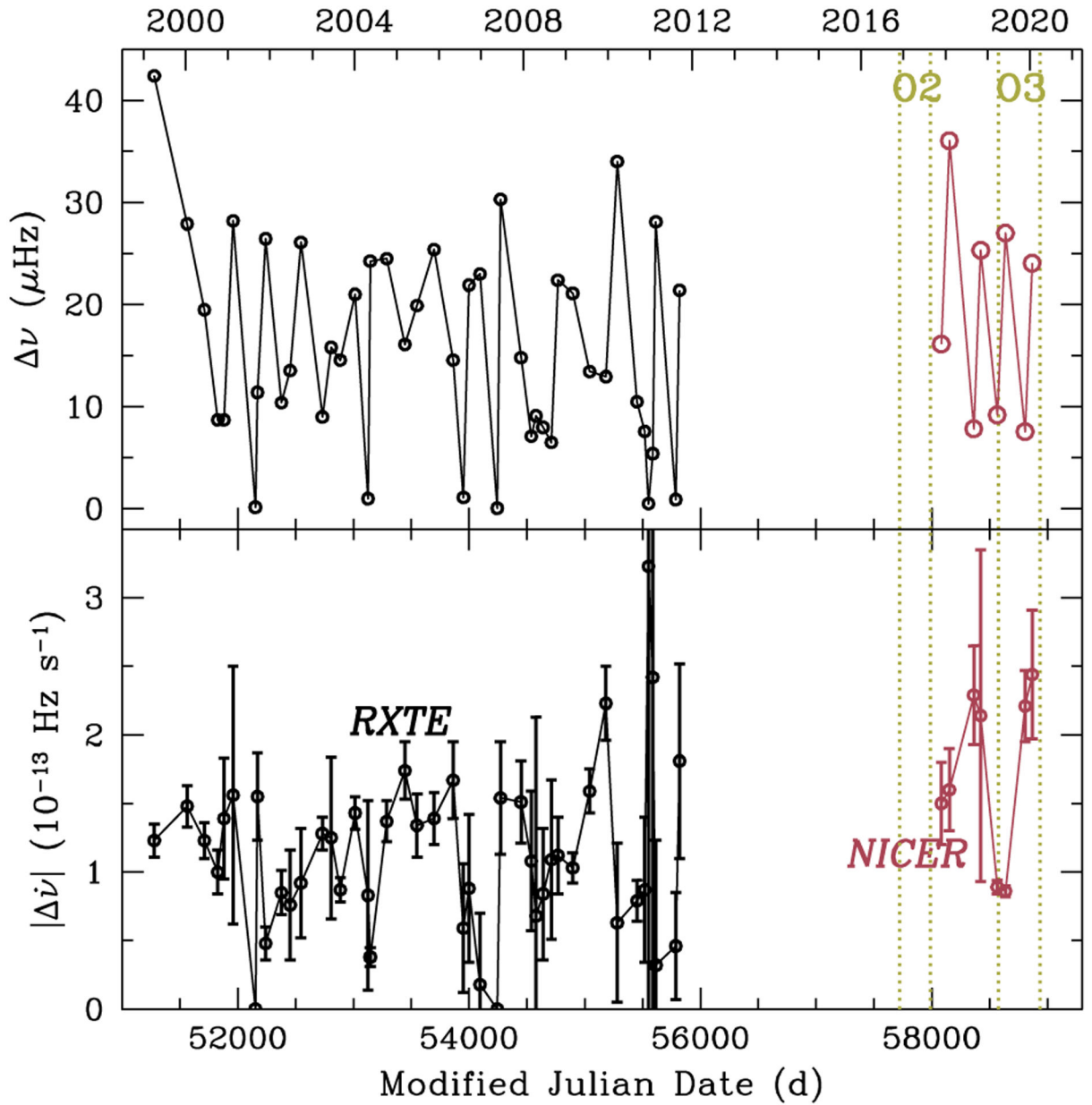
Figure 6.

Braking index n_{ig} calculated from spin parameters of each segment between glitches as a function of time since last glitch. Large and small circles denote NICER and RXTE values, respectively, with the latter taken from Tables 1 and 2 of Antonopoulou et al. (2018). Errors in n_{ig} are 1σ uncertainty. Horizontal dotted lines indicate braking index $n = 3, 5, 7$, which are expected for pulsar spin-down due to electromagnetic dipole radiation, gravitational-wave emitting ellipticity, and gravitational-wave emitting r-mode oscillation, respectively (see Section 5.2). Short and long-dashed lines indicate exponential decay to $n = 3$ with best-fit timescale of 26 d and to $n = 7$ with best-fit timescale of 20 d, respectively.
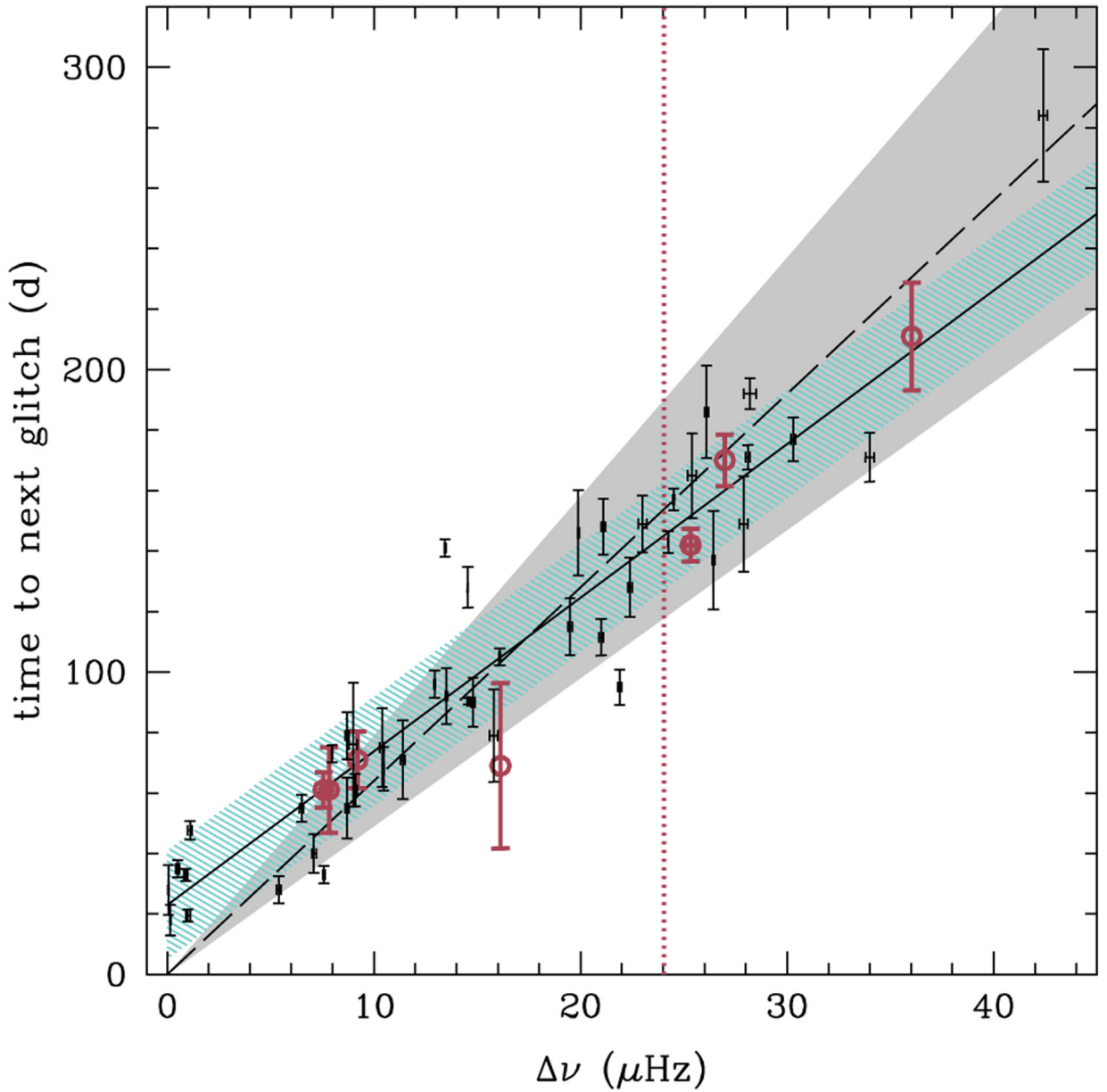
Figure 7.
Fractional glitch magnitude v/v shown as a cumulative sum over each previous glitch. RXTE values are from Table 2 of Antonopoulou et al. (2018), Dashed line indicates a line with a slope of 8.84×10^{-7} yr^{-1}, which is the glitch activity $A_g \equiv \sum_i (v/v)_i/t_{obs}$ from RXTE data, where t_{obs} is time over which the pulsar is monitored; note that $A_g = 8.88 \times 10^{-7}$ yr^{-1} for the combination of RXTE and NICER glitches. NICER values are offset by $v/v = 16.5 \times 10^{-6}$, i.e., value of dashed line at the epoch of NICER segment 0 at MJD 58020.
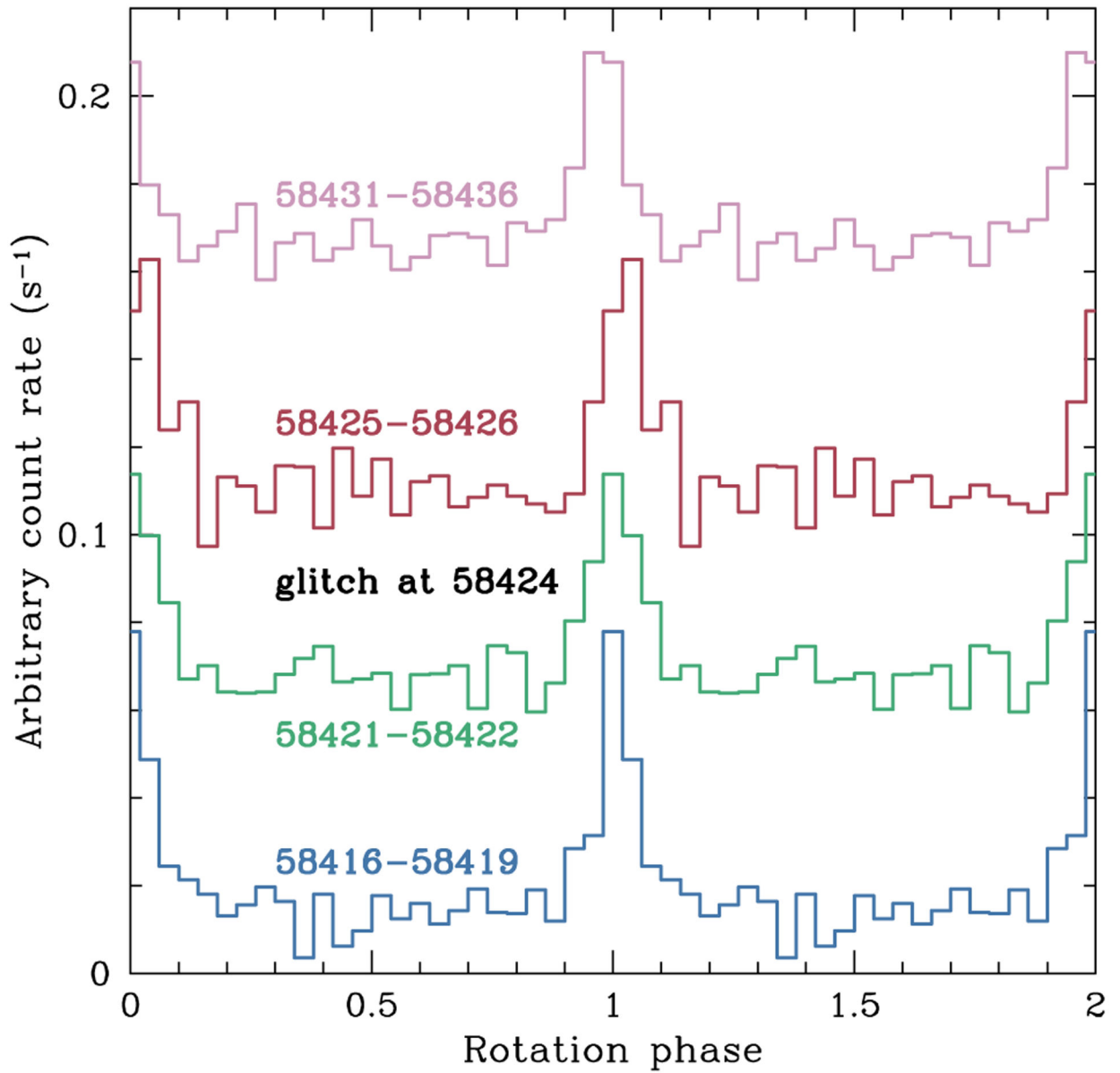
Figure 8.
Glitch ν (top) and $\dot{\nu}$ (bottom) as functions of time. Large and small circles denote NICER and RXTE values, respectively, with the latter taken from Table 2 of Antonopoulou et al. (2018). Errors in bottom panel are 1σ uncertainty, while errors are not shown in top panel because they are smaller than the circles. Vertical dotted lines denote the start (MJD 57722, 2016 November 30) and end (MJD 57990, 2017 August 25) of the second observing run (O2) and start (MJD 58574, 2019 April 1) and end (MJD 58935, 2020 March 27) of the third observing run (O3) of LIGO/Virgo.

Figure 9.
Time to next glitch as a function of glitch size *v*. Circles with errors are NICER values, and points with errors are RXTE values, which are from Table 2 of Antonopoulou et al. (2018). Vertical dotted line indicates the size of glitch 8, which is the most recent NICER-detected glitch and for which the time to next glitch is not known yet. Errors in *v* are 1σ uncertainty. Solid and dashed lines show a linear fit of NICER and RXTE data with time to next glitch = 6.4 d (*v*/μHz) and time to next glitch = 23 d + 5.08 d (*v*/μHz), respectively, while shading shows correlation regions which fit 68 percent of glitches (see Section 4.2).

Figure 10.
Pulse profiles of PSR J0537–6910 in the 1–7 keV band, folded at the ephemeris from Tables 1 and 2, from earliest date at the bottom to latest date at the top. Two rotation cycles are shown, with 25 bins per cycle, and each profile is arbitrarily shifted in count rate for clarity. Labels indicate MJD of data used to construct profile and epoch of glitch 4 (at MJD 58424).

Table 1.

PSR J0537−6910 timing model parameters for segments between glitch epochs. Number in parentheses is 1σ uncertainty in last digit.

Segment	Epoch (MJD)	Start (MJD)	End (MJD)	TOAs	ν (Hz)	$\dot{\nu}$ $(10^{-10}$ Hz s$^{-1})$	$\ddot{\nu}$ $(10^{-20}$ Hz s$^{-2})$	n_{ig}	Residual RMS (μs)	χ^2/dof
0	58020	57984.5	58057.5	4	61.924374260(2)	−1.99547(5)	[1]^a	—	66.14	3.1
1	58124	58108.1	58141.6	3	61.922597203(3)	−1.9961(3)	[1]^a	—	1.158	—^{b}
2	58255	58163.0	58348.8	21	61.920372999962(9)	−1.996977(2)	0.56(1)	8.7(2)	123.5	4.4
3	58399	58377.5	58422.2	11	61.917896251(3)	−1.99689(2)	5.9(6)	90(10)	56.39	1.2
4	58493	58426.1	58560.6	13	61.916299559(4)	−1.997261(8)	0.81(8)	13(1)	250.8	20
5	58600	58571.3	58629.3	7	61.914462421(2)	−1.99740(3)	[1]^a	—	98.49	3.3
6	58723	58645.5	58804.5	16	61.912366620(2)	−1.997289(4)	0.88(3)	13.7(4)	142.7	5.9
7	58836	58810.0	58862.9	6	61.910424210(6)	−1.99742(4)	5.8(9)	90(10)	81.92	4.7
8	58918	58872.5	58964.4	14	61.909033102(3)	−1.99765(1)	1.4(1)	22(2)	138.4	6.9

$^a\ddot{\nu}$ is fixed at 10^{-20} Hz s^{-2} (see text).

^{b}No fit performed (see text).

Table 2.

PSR J0537−6910 glitch parameters. Number in parentheses is 1σ uncertainty in last digit.

Glitch	Glitch epoch (MJD)	ϕ (cycle)	ν (μHz)	$\dot{\nu}$ (10^{-13} Hz s^{-1})	$\ddot{\nu}$ (10^{-20} Hz s^{-2})
1	58083(25)	−0.016(8)	16.132(2)	−1.5(3)	—
2	58152(11)	0.47(1)	36.035(6)	−1.6(3)	−0.44(1)[a]
3	58363(14)	0.17(5)	7.83(5)	−2.3(4)	5(1)
4	58424(2)	−0.35(23)	25.3(3)	−2(1)	−5(2)
5	58566(5)	−0.32(2)	9.21(2)	−0.89(5)	—
6	58637(8)	0.03(2)	26.99(1)	−0.86(4)	−0.12(3)[a]
7	58807(3)	0.31(2)	7.57(3)	−2.2(3)	5(1)
8	58868(5)	0.06(6)	24.04(8)	−2.4(5)	−4(1)

[a]In the preceding segment, $\ddot{\nu}$ is fixed at 10^{-20} Hz s^{-2} due to a low number of TOAs (see Table 1). $\ddot{\nu}$ is the difference between this fixed value and $\ddot{\nu}$ in the next segment.